

Bi-functional S-Doped Ni Catalysts on Copper Foams with Enhanced Electrocatalytic Performance and Excellent Stability for Electrocatalytic Water Splitting

Suyang Feng¹, Ruidong Xu^{1,2,*}, Xuanbing Wang¹, Wenbin Wang², Chen Chen², Ao Ju², Ying Zhang², Yan Ju²

¹ State Key Laboratory of Complex Nonferrous Metal Resources Clean Utilization, Kunming University of Science and Technology, Kunming 650093, China

² Faculty of Metallurgical and Energy Engineering, Kunming University of Science and Technology, Kunming 650093, China

*E-mail: rdxupaper@aliyun.com

Received: 20 October 2019 / Accepted: 29 December 2019 / Published: 10 February 2020

The low-cost and energy-efficient catalysts for water splitting are crucial for the sustainable development and renewable energy. The abundant reserves of nickel sulfides have been expected to serve as the precious metal-free materials for the oxygen evolution reaction (OER) or hydrogen evolution reaction (HER). In this research, a bi-functional S-doped Ni films on three-dimensional (3D) porous copper foams (marked as NiS_x/CF) were prepared by a one-step potentiostatic electrodeposition approach in an ethaline solution containing 40mmol NiCl₂·6H₂O and 20mmol CH₄N₂S. The phase structures, surface elemental valence state, and surface microstructures were observed by X-ray diffraction (XRD), X-ray photoelectron spectrum (XPS), and field-emission scanning electron microscope (FE-SEM). The electrocatalytic performances were measured by linear sweep voltammetry (LSV), Cyclic Voltammetry (CV), Electrochemical impedance spectra (EIS) and ISTEP Multi-Current Steps. The doping of S into Ni grains and three-dimensional porous structure were found to induce more abundant active sites, significantly improving the water splitting electrolytic activity in alkaline media. The NiS_x/CF catalyst exhibits the lowest overpotential of OER with 302mV at 20 mA·cm⁻² and the lowest overpotential of HER with 146mV at 10 mA·cm⁻². When used in electrocatalytic water splitting, it displays a low cell voltage usage of 1.532V at 20mA cm⁻² in 1 M KOH. Furthermore, it maintained excellent stability under multiple potentials. Therefore, this research offers a simple synthesis route to fabricate precious metal-free OER and HER Bi-functional catalysts for electrocatalytic water splitting.

Keyword: S-doped Ni; copper foam; catalyst; electrocatalytic activity; electrocatalytic water splitting

1. INTRODUCTION

The development of environmentally-friendly, low cost, long-term, and steady catalysts plays an important part in the field of new energy [1-3]. The use of reproducible energy like solar power, tidal power, and wind power has been repeatedly encouraged [4-7]. However, the lack of suitable energy storage technologies and their consequential high cost have hindered the application of these energy sources [8]. Hydrogen, one of the most prospective sources of energy that is neat and effective, is used as a substitute for the traditional non-renewable energy sources, for sustainable development [9]. At present, the main source of hydrogen is prepared by electrocatalytic water splitting, [$\text{H}_2\text{O} (\text{l}) = \text{H}_2 (\text{g}) + 1/2 \text{O}_2 (\text{g})$; $1/2\Delta G^\circ = +237200 \text{ J/mol}$, $\Delta E^\circ = 1.23\text{V}$ versus reversible hydrogen electrode (RHE)], which is a reverse process of fuel cell reactions [10] that involves the anodic oxygen evolution reaction and cathodic hydrogen evolution reaction [4].

The overall reaction pathway for the OER and HER in alkaline solutions is shown in Table 1. As shown in Table 1, E_c^0 and E_a^0 are the equilibrium half-cell potentials for the HER and OER at 1 atm and 298 K [11-14]. The theoretical water-splitting voltage is 1.23 V; however, the required practical voltage is from 1.40 V to 2.0 V owing to the existence of various resistances [15]. The OER and HER reaction result in the adsorption and removal of oxygen and hydrogen atoms, and these are competitive relationships. An ideal catalyst should have a balance between the binding and releasing of adsorbed intermediates such as O^* , OH^* , OOH^* , and H^* [16]. Therefore, an ideal HER or OER catalyst should satisfy the following two conditions. First, it should display an admirable activity providing a low overpotential, leading to higher current density. Second, it must possess a long-term stability.

Table 1. Overall reaction pathway for OER and HER in alkaline solutions

Reaction types	Overall reactions	Reaction pathway
OER	$4\text{OH}^- = \text{O}_2 + 2\text{H}_2\text{O} + 4\text{e}^-$ $E_c^0 = (1.23 \text{ V} - 0.059 \text{ pH}) \text{ V}$ vs. RHE	$* + \text{OH}^- = *\text{OH} + \text{e}^-$ $*\text{OH} = *\text{O} + \text{H}^+ + \text{e}^-$ $*\text{O} + \text{H}_2\text{O} = *\text{OOH} + \text{e}^-$ $*\text{OOH} + \text{OH}^- = *\text{O}_2 + \text{e}^-$
HER	$2\text{H}_2\text{O} + 2\text{e}^- = \text{H}_2 + 2\text{OH}^-$ $E_a^0 = (0 - 0.059 \text{ pH}) \text{ V}$ vs. RHE	$\text{H}_2\text{O} + \text{e}^- = \text{H}^* + \text{OH}^-$ $\text{H}_2\text{O} + \text{e}^- + \text{H}^* = \text{H}_2 + \text{OH}^-$ Or $2\text{H}^* = \text{H}_2$

Where, * stands for active site on the surface of catalyst, O^* , OH^* , OOH^* and H^* are the adsorbed intermediates.

Usually, IrO_2 and RuO_2 are used as the standard OER and HER catalysts owing to the high electrocatalytic activity in the alkaline solutions. However, these expensive metal oxides are not adaptive for the large-scale applications [16-18]. Immense research efforts have been devoted to the development of low-cost OER and HER catalysts based on Cu, Ni, Fe, Cr, Mo, and their relevant sulfides/oxides [19].

Typically, for the OER catalysts, a NiCo nanosheet is synthesized by a topochemical approach method, delivering an overpotential of 332 mV at 10 mA cm⁻² [20]. NiMo HNRs/TiM was prepared by a template-assisted electrodeposition method, displaying an overpotential of 310 mV at 10 mA cm⁻² [21]. For HER catalysts, N-MoP-850 was synthesized by a thermal reduction method, which delivered an overpotential of 156 mV at 10 mA cm⁻² [22]. Mn-Ni₃S₂ on the Ni foam substrate exhibited an overpotential of 156 mV at 10 mA cm⁻² [23]. Another Ni₃S₂ nanorod was also synthesized by a hydrothermal method and delivered an overpotential of 200 mV at 10 mA cm⁻² [24].

In our research, the bi-functional S-doped Ni catalysts are prepared on the three-dimensional porous copper foams by a one-step potentiostatic electrodeposition, and the relationships among the S-doping, microstructures and electrocatalytic activity are discussed. Notably, the doping of S into Ni grains and three-dimensional porous structure induce more abundant active sites, thereby significantly improving the OER or HER electrolytic activity in alkaline media. The NiS_x/CF exhibits the lowest overpotential of OER with 302 mV at 20 mA·cm⁻² and the lowest overpotential of HER with 146 mV at 10 mA·cm⁻². When used in electrocatalytic water splitting, it displays a lower cell voltage of 1.532 V at 20 mA cm⁻² in 1 M KOH. Moreover, it also shows excellent characteristic of maintaining stability under multiple potentials. Therefore, NiS_x/CF may be an ideal OER and HER Bi-functional catalyst for electrocatalytic water splitting.

2. EXPERIMENTAL SECTIONS

2.1 Electrochemical preparation of NiS_x/CF catalysts

Analytical grade chemical reagents, including ethylene glycol (EG), choline chloride (ChCl, 99%), nickel chloride hexahydrate (NiCl₂·6H₂O, 98%), thiourea (CH₄N₂S, 99%) and potassium hydroxide (KOH, 95%), were used in the experiment. Ethaline with 40 mL was composed to mixing ChCl and EG at a molar ratio of 1:2. Thereafter, S-doped Ni films (marked as NiS_x/CF) were prepared by a one-step electrodeposition approach in ethaline containing 40 mmol NiCl₂·6H₂O and 20 mmol CH₄N₂S. At 333 K, the voltage at constant potential was -0.65 V (vs. Ag wire). Typically, the electrodeposition of Ni/CF and NiS_x/CF electrodes is performed in a standard three-electrode cell with a porous copper foam (Type: PPI, 1 cm×2 cm, 1 mm thickness) as the working electrode. The Pt column acts as the counter electrode and the silver wire as the reference electrode. Prior to each deposition, reference electrode, counter electrode, and porous copper foam substrate were pretreated by ultrasound and rinsed with absolute ethanol and 1 vol% HCl. It was then washed with deionized water and finally vacuum dried. After the deposition, the samples were washed again with deionized water and dried for further characterization.

2.2 Structural and microstructure characterization

The phase structures of pure Ni, NiS_x deposits were probed using powder X-ray diffraction (XRD) patterns recorded on the Rigaku D/Max-2200 diffractometer with Cu K_α radiation. X-ray

photoelectron spectroscopy (XPS) analysis was studied using the PHI 5500 X-ray photoelectron spectroscope. The microstructures, and chemical compositions of porous copper foam or Ni, NiS_x deposits were measured using field-emission scanning electron microscope (FE-SEM) recorded on a FEI Nova, Nano SEM 450 equipped with energy-dispersive X-ray (EDS) under 10 KV, respectively.

2.3 Electrochemical measurements

The linear sweep voltammetry (LSV), open circuit potential (OCP), cyclic voltammetry (CV), electrochemical impedance spectroscopy (EIS), and Multi-Current Steps (ISTEP) of NiS_x/CF, Ni/CF, and pure CF were performed using the PARSTAT2273 electrochemical workstation. For these electrochemical measurements, a standard three-electrode system was used, and the prepared sample was used as the working electrode. The Ag/AgCl electrode was used as the reference electrode and the Pt column was used as the counter electrode. The distance between the reference electrode and the working electrode was approximately 5mm.

All the OER or HER potentials appearing in this study were converted to vs. reversible hydrogen electrode (RHE) according to the eq [10]:

$$E (\text{vs. RHE}) = E (\text{vs. Ag/AgCl}) + 0.197 + 0.059 \times \text{pH} \quad [1]$$

The linear portions of Tafel polarization curves were inserted in the eq [25]:

$$\eta = b \log j + a \quad [2]$$

where j is the current density, η denotes the overpotential, and b is the Tafel slope.

The electrochemical active surface areas (ECSAs) can be estimated by using capacitance (C). To compare the ECSAs of different catalysts, CVs were recorded at a window from 1.11V to 1.21 V (vs RHE) with different scan rates between 20 and 200 mV s⁻¹. The ECSAs were obtained by the Eq [26, 27]:

$$\text{ECSA} = \frac{C}{0.04 \text{mF cm}^{-2} \text{ per cm}^{-2}} \quad [3]$$

The corresponding current density (j) between the anode and cathode $1/2(j_{\text{anodic}} + j_{\text{cathodic}})$ at 1.16 V versus RHE, linear slope was calculated as C_{dl} . Through Cyclic Voltammetry, electric double layer curves were obtained from open circuit potential (OCP) \pm 0.05 V. EIS tests were performed at the frequency range from 0.1 Hz to 10 KHz under a constant potential of 0.96 V versus RHE. Testing Stability with Multi-Current Steps (ISTEP), the current successively rose from 10 to 80 mA cm⁻² at the rate of 10 mA cm⁻² per 500 s.

3. RESULTS AND DISCUSSION

3.1 Microstructures and phase structures

The pure nickel deposit and S-doped nickel deposit (NiS_x) with a Ni:S atomic ratio of 1: 0.25 was grown on the CF substrates, and the introduction of the S atoms into these nickel deposits was

realized through the addition of thiourea in the electrolyte. To avoid the influence of the CF substrate on the phase structures of the deposits, the pure nickel and NiS_x deposits were stripped directly from the surface of the CF substrate after a one-step potentiostatic electrodeposition, and they were measured by an XRD diffractometer; the results are shown in Fig. 1(a).

Fig. 1(a) shows that the XRD pattern for the pure nickel deposit matches well with face-centered cubic Ni phases at 2θ of 44.49°, 51.84°, and 76.38° (JCPDS No. 87 – 0712), and their corresponding diffraction crystal planes are (111), (200) and (220). Compared to the pure nickel deposit, the S-doped nickel deposit (NiS_x) shows a left shift in the diffraction peaks at the following diffraction crystal planes of (111), (200) and (220), and their left shift angles are 0.14° at (111), 0.22° at (200), and 0.34° at (220), respectively, as shown in Fig. 1(b), Fig. 1(c), and Fig. 1(d), displaying that the partial in Ni lattices are substituted by the doped S atoms [28-30], leading to the compaction of the unit cell [31] and the left shift of the diffraction peaks. An interstitial compound can be formed when the atomic radius ratio of a metal to a nonmetal exceeds 0.59. The atomic radius of S (1.04 Å) is smaller than that of Ni (1.15 Å), and the ratio of the atomic radius S to Ni is about 0.904; therefore, NiS_x deposit on CF substrate exists in the forms of an interstitial compound and not a solid solution. It is also obvious from Fig. 1(a) that the diffraction peak intensity of the pure nickel deposit is higher than that of the NiS_x deposit at diffraction crystal planes of (111), (200), and (220), displaying that the incorporation of S atoms into the lattices of nickel networks hinders the growth of the Ni atoms at the aforementioned three diffraction crystal planes. These results confirm the incorporation of S atoms into the lattices of nickel networks achieved via a one-step electrodeposition [32].

An X-ray photoelectron spectrum (XPS) is employed to research the elemental surface constituents and valence state of the catalysts (Fig. 1e-g). It can be observed from Fig. 1(e) that the peaks in the XPS spectrum show the presence of Ni, S, Cl, O, and C elements. The presence of Cl, O, and C may have come from the surface of the sample and the trace solvent residues. The XPS spectra of Ni 2p and S 2p regions of the NiS_x/CF sample are shown in Fig. 1(f, g). Fig. 1f shows that four peaks. The two strong peaks at 856.5 eV and 873.9 eV correspond to the Ni 2p_{3/2} and Ni 2p_{1/2} electronic configurations of the Ni²⁺ species on the surface of the catalyst, along with the two satellite peaks at 862.1 eV and 879.9 eV [33,34]. As can be seen from Fig. 1(f), Ni 2p_{3/2} and Ni 2p_{1/2} identified that the splitting peaks and corresponding binding energy at the combined state were 856.5 eV and 873.9 eV [19]. As it is easy to be oxidized when NiS_x meets oxygen, the XPS spectrum of the Ni binding energy of 856.5 eV is probably due to NiS_x being partially oxidized to NiSO₄ [35,36].

In the S 2p in spectrum Fig. 1(g), the peaks at 163.4 eV (S 2p_{3/2}) and 164.5 eV (S 2p_{1/2}) are attributed to the binding energy for the sulfide [37]. The separation of the S 2p_{3/2} and S 2p_{1/2} spin-orbit components was kept about 1.2eV Fig. 1(g) presents the S 2p region, which further confirmed the substitution of S. Meanwhile, the peak located at 168.5 eV was assigned to S-O bond caused by surface oxidation in the air. Hence, these two different forms of sulfur originate from the disproportionation during the sulfuration [38,39]. These results indicate that S and Ni form NiS_x compounds and a strong electronic interaction between S and Ni in NiS_x leads to an increase in the electronic density of the catalyst at the surface [38].

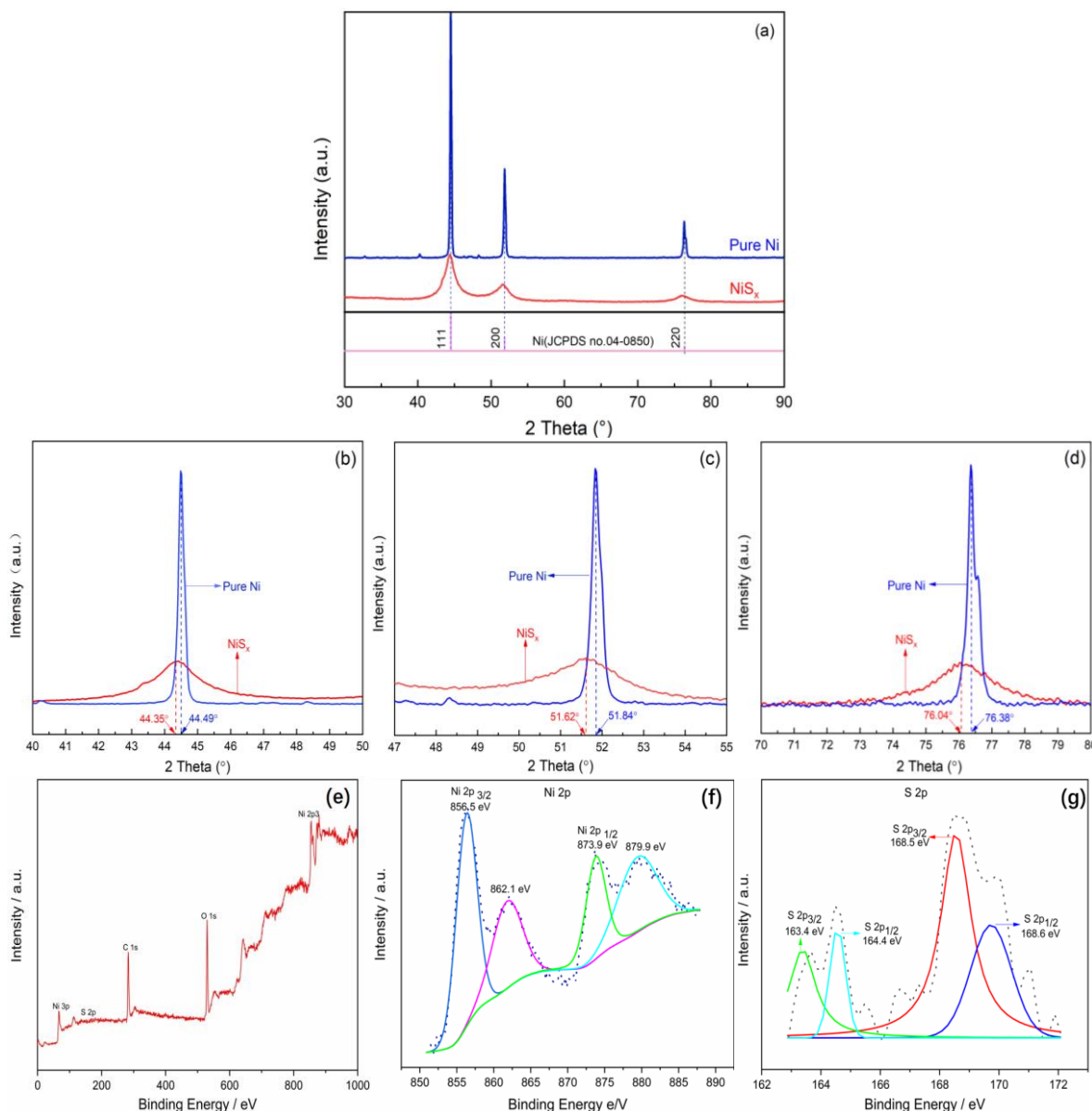
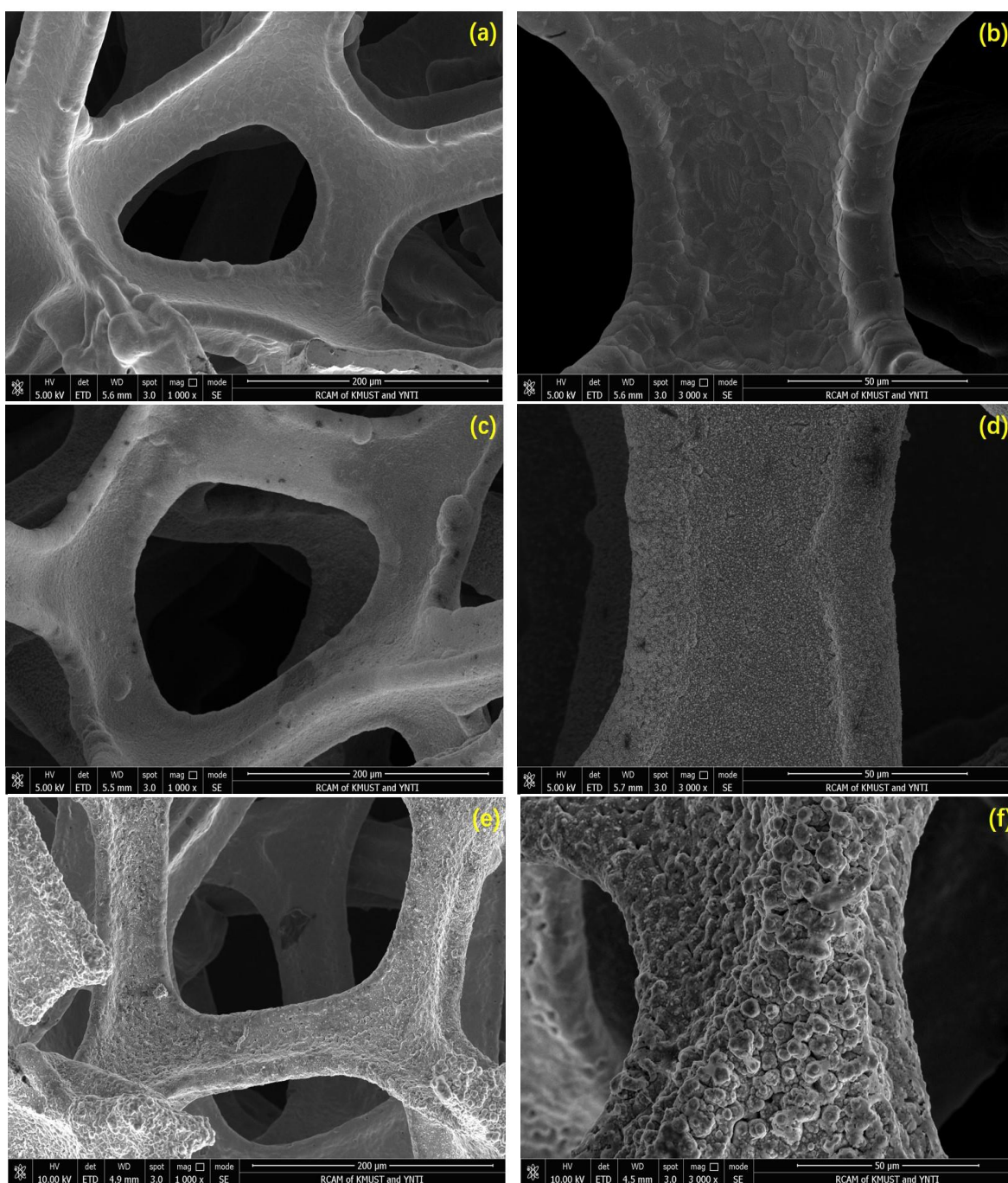


Figure 1. (a) XRD patterns of NiS_x and pure Ni prepared at -0.65V vs. Ag wire with deposition time of 40 min at 333 K in 40 mM NiCl₂·6H₂O/ethaline and 40 mM NiCl₂·6H₂O+ 20mM CH₄N₂S/ethaline, respectively. The typical peak left shift of (b) 2θ: 44.39° at (111), (c) 51.84 at (200) and (d) 76.38° at (220)after S doping. (e) XPS survey spectrum for NiS_x/CF. XPS spectra in the (f) Ni 2p, (g) S 2p regions for NiS_x/CF.

Figure 2 indicates field-emission scanning electron microscopy (FE-SEM) images of the NiS_x/CF catalyst and copper foam. As shown in Fig. 2(a, b), the CF substrate has a 3D porous structure and a relatively smooth surface. The higher the conductivity of the CF substrate is, the faster the electron migration of the system is, hence, the more favorable it is for the reaction. The SEM images of Ni/CF are shown in Fig. 2(c, d). The Ni deposit is prepared on the surface and uniformly covers the surface of the CF substrate. Nickel has a face-centered cubic crystal structure. The SEM images of NiS_x/CF are shown in Fig. 2(e, f). It can be observed from Fig. 2(e, f) that the NiS_x deposit is prepared on the outside and the inside of the CF substrate, and some regular micropores exist on the surface and inside of the synthesized deposits. Particularly, a microsphere-like morphological structure is formed. The

microsphere-like morphological structure can help to reduce the internal stress generated in the structure providing a smooth pathway for the penetration of the electrolyte and an adequate contact area between the active positions and reactants. Furthermore, the structure strengthens the bond between the prepared deposits and the CF substrate to guarantee outstanding physical and electrocatalyst performance. As mentioned earlier, it can be seen that the electrochemical active surface areas of NiS_x/CF are larger than those of pure CF.

The EDS mapping images in Fig. 2(g-i) indicate that the nickel (Ni) sulfur (S) elements have been obtained and are distributed uniformly in the deposit with unknown phase structure. Fig. 2(h) show that the peak of nickel, sulfur and copper are clearly visible displaying that the NiS_x deposit on the CF substrate has been successfully fabricated by an electro-deposition method.



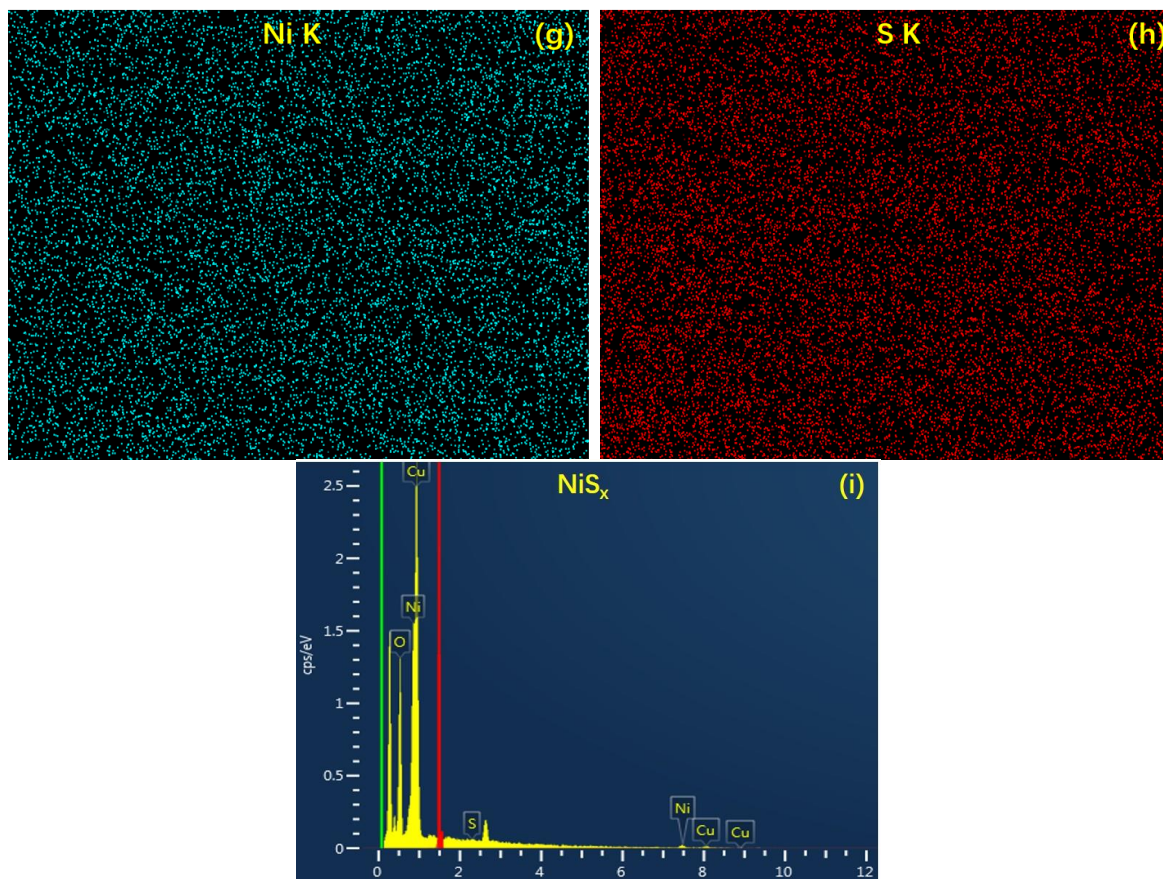


Figure 2. (a,b) SEM image of CF substrate. (c,d) SEM images of Ni/CF. (e,f) SEM images of NiS_x/CF. (g,h) Ni and S elemental mapping images of NiS_x/CF. (i) EDS spectrum of NiS_x/CF

3.2 OER and HER electrochemical properties

This section describes the OER and HER reactions and their potentials vs RHE during the electrocatalytic water splitting. The two reactions can be grouped into two reversible reaction couples. One is the oxygen evolution reaction (OER) and it illustrates the equilibrium potential of 1.23V vs RHE (hydrogen electrode). The other one is the hydrogen evolution reaction and it illustrates the equilibrium potential of 0V vs RHE. The theoretical overpotential of OER (η^{OER}) and HER (η^{HER}) at benchmark condition is defined as follows [39,40]:

$$\eta^{\text{OER}} = (G^{\text{OER}}/e) - 1.23\text{V} \quad [4]$$

$$\eta^{\text{HER}} = (G^{\text{HER}}/e) - 0\text{V} \quad [5]$$

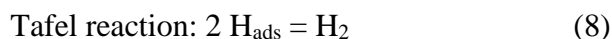
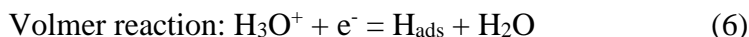
The electrocatalytic activity of the porous NiS_x/CF OER prepared is assessed in 1.0 M KOH by steady-state linear scanning voltammetry (LSV) with a scan rate of 5 mV s⁻¹. The NiS_x and pure Ni are deposited on a copper foam electrode according to the measurement of their electrochemical properties. Fig. 3(a) shows that the current densities of the corresponding NiS_x/CF, Ni/CF, and Pure CF at 1.7 V are 80.6 mA cm⁻², 32.5 mA cm⁻², and 2.6 mA cm⁻², respectively. Some oxidation reaction occurs below the current density of 20 mA cm⁻². Fig. 3(b) shows the NiS_x/CF catalyst not only displays a lower overpotential of 302 mV to achieve a current density of 20 mA cm⁻² compared to the other Ni/CF catalyst

(428 mV), but also a lower overpotential to achieve a current density of 10 mA cm⁻² compared to the typical material such as, NiCo nanosheets (332 mV) [20] and NiMo HNRs/TiM (310 mV) [21]. A more detailed comparison is given in Table 2. The catalysts are divided into classes, namely, ideal (200-300 mV), excellent (300-400 mV), good (400-500 mV) and satisfactory (beyond 500 mV) [14]. Hence, it can be concluded that NiS_x/CF exhibits excellent catalytic performance.

Table 2. OER activity, types of solutions, electrodes, and overpotential of typical materials in the literatures.

OER Catalysts	Solution	Electrode	Over potential(mv)	Ref
NiS _x /CF	1 M KOH	Cu-foam	302 @20mAcm ⁻²	In the text
NiCo nanosheets	1 M KOH	GC	332 @10mAcm ⁻²	[20]
NiMo HNRs/TiM	1 M KOH	TiM	310 @10mAcm ⁻²	[21]
IrO ₂	1 M KOH	GC	338 @10mAcm ⁻²	[41]
IrO ₂ /C	0.1 M KOH	GC	370 @10mAcm ⁻²	[12]
Ni ₂ Fe ₈ -LDH	1 M KOH	-	349 @20mAcm ⁻²	[42]
NiS _x /NC	1 M KOH	NC	371 @10mAcm ⁻²	[43]

Fig. 3(c) shows that we compared the catalytic performance at three different overpotentials. The NiS_x/CF catalyst delivered current densities of 19.77 mA cm⁻², 50.10 mA cm⁻² and 94.74 mA cm⁻² at 300 mV, 400 mV and 500 mV respectively, which are better comparison of Ni/CF and pure CF. As expected, NiS_x/CF catalyst exhibits excellent OER activity, while the deposited Ni/CF and foam copper exhibits poor OER activity. Tafel slope is used to show the reaction mechanism and kinetics of the catalysts for OER. The reaction path is composed of proton adsorption and removal on the catalyst surface to form H_{ads}, followed by H₂ formation and desorption [44]. This includes the Volmer mechanism, the Heyrovsky mechanism and the Tafel mechanism, detailed as follows [22]:



The Tafel slope of the catalyst NiS_x/CF (120.1 mV dec⁻¹) is lower than that of the Ni/CF (178.2 mV dec⁻¹), indicating more favorable catalytic kinetics for NiS_x/CF. The rate-determining step will be identified as the Tafel, Heyrovsky, or Volmer step, depending on the Tafel slope measurement is 30, 40, or 120 mV/dec, respectively [45]. NiS_x/CF led to a Tafel slope of 120.1 mV dec⁻¹, suggesting that the oxygen evolution reaction is controlled by Volmer reaction (H₃O⁺ + e⁻ = H_{ads} + H₂O) [25].

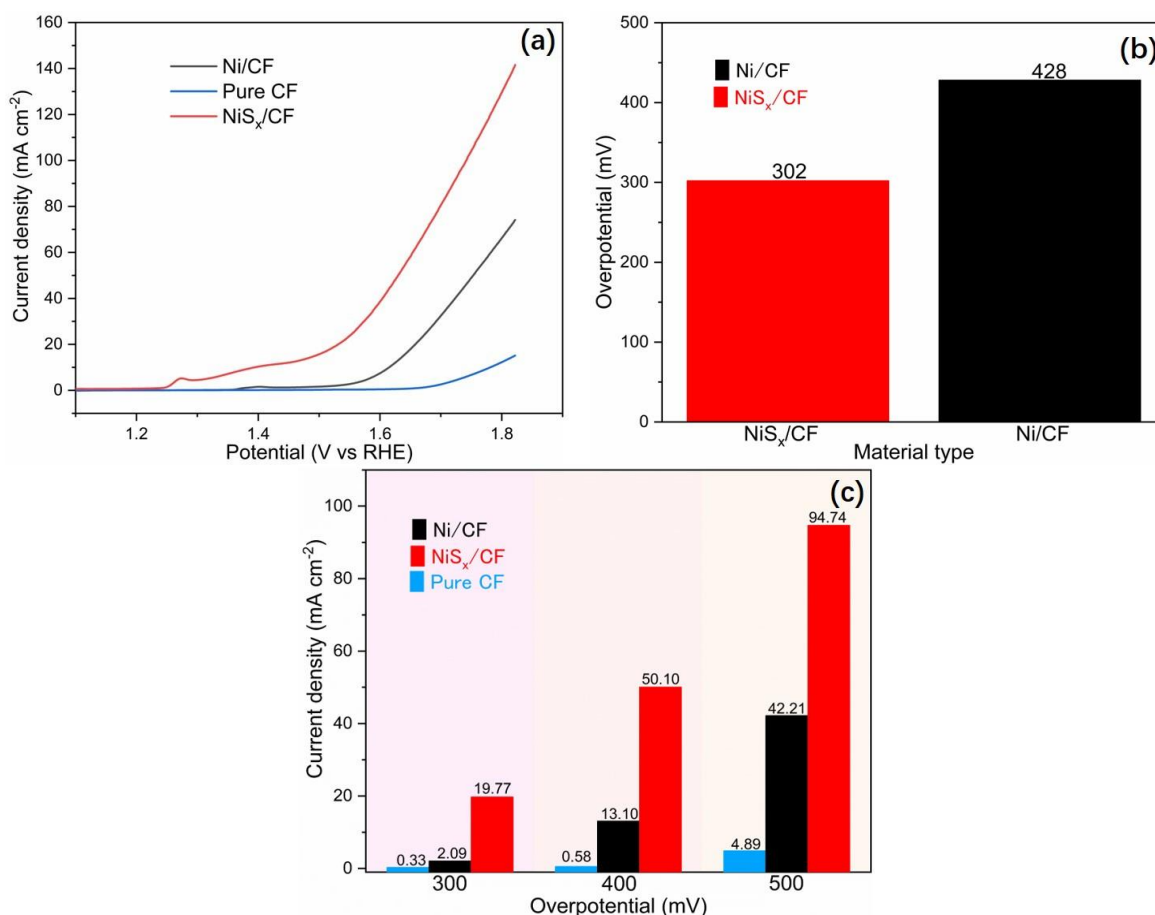


Figure 3. (a) Anodic polarization curves of pure CF, Ni/CF and NiS_x/CF. (b) OER overpotentials for pure CF, Ni/CF and NiS_x/CF. (c) Comparison of current density at different OER overpotentials for pure CF, Ni/CF and NiS_x/CF.

To testify the applicability of these catalysts in overall water splitting course, Fig. 4(a) shows that the NiS_x/CF catalyst delivered very good catalytic activity for the HER, which is better than that of Ni/CF and pure CF. The current densities of the corresponding NiS_x/CF, Ni/CF and Pure CF at -0.4 V are 103.5 mA cm⁻², 78.1 mA cm⁻², and 5.2 mA cm⁻², respectively. It is worth noting that some fluctuation in the current density was observed, which can be ascribed to the accumulation and release of H₂ bubbles on the catalyst surface [11].

Fig. 4(b) shows that the current densities of NiS_x/CF, Ni/CF and pure CF can approach 10 mA cm⁻² at an overpotential of 146 mV, 171 mV and 531 mV respectively. The overpotential of the catalyst is reduced with the presence of Ni and S element at different degrees. Meanwhile, the NiS_x/CF overpotential achieves a current density of 10 mA cm⁻² lower than typical material such as N-MoP-850 (156 mV) [22] and Mn-Ni₃S₂ (152 mV) [23]. Other detailed comparison is given in Table 3.

Table 3. HER activity, types of electrodes, solutions and overpotential of typical materials reported in the literatures.

HER Catalysts	Solution	Electrod e	Over potential(mv)	Ref
NiS _x /CF	1 M KOH	Cu foam	146 @10mAcm ⁻²	In the text
N-MoP-850	1 M KOH	-	156 @10mAcm ⁻²	[22]
Mn-Ni ₃ S ₂	1 M KOH	Ni foam	152 @10mAcm ⁻²	[23]
Ni ₃ S ₂ nanorod	1 M KOH	-	200 @10mAcm ⁻²	[24]
Fe(OH) ₃ Cu(OH) ₂	1 M KOH	Cu foam	365 @10mAcm ⁻²	[46]
Ni-P NPs	1 M KOH	Cu foam	360 @10mAcm ⁻²	[47]
NiS _x microsphere	1 M KOH	Ni foam	158 @10mAcm ⁻²	[48]

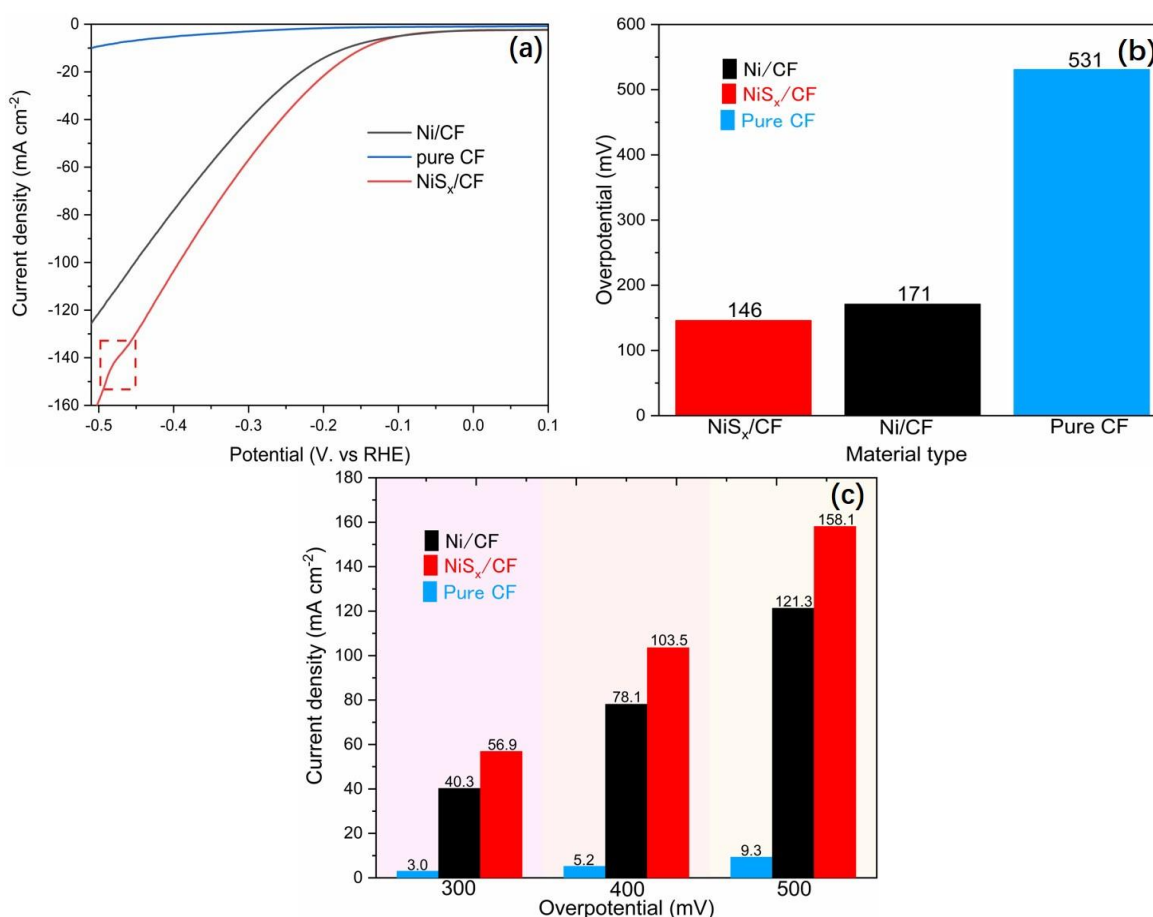
**Figure 4.** (a) Anodic polarization curves of pure CF, Ni/CF and NiS_x/CF. (b) HER overpotentials for pure CF, Ni/CF and NiS_x/CF. (c) Comparison of current density at different OER overpotentials for pure CF, Ni/CF and NiS_x/CF.

Fig. 4(c) shows the comparison of current densities of the three materials under different overpotentials at 300 mV, 400 mV, and 500 mV. The NiS_x/CF catalyst displays current density higher than the Ni/CF and pure CF catalysts. The NiS_x/CF catalyst deliver current densities of 56.9 mA cm⁻², 103.5 mA cm⁻², and 158.1 mA cm⁻² at 300 mV, 400 mV and 500 mV respectively, which are much better

than those of Ni/CF and pure CF. Hence, NiS_x/CF catalyst exhibits excellent HER activity, while deposited Ni/CF and foam copper exhibits poor HER activity. The kinetic of HER processes of NiS_x/CF catalysts is further investigated from the derived Tafel slope. Tafel slopes for NiS_x/CF, Ni/CF and pure CF are about 156.2, 198.9, 368.9 mV dec⁻¹, respectively, suggesting that the hydrogen evolution reaction is controlled by a fast discharge Volmer reaction and relatively slow desorption Heyrovsky reaction [25].

3.3 Overall Water Splitting

Fig. 5(a,b) results demonstrate that the doping of S source indeed significantly advanced the overall water splitting performance of the NiS_x/CF catalyst. It displays only a cell voltage of 1.532 V is required to achieve a current density of 20 mA cm⁻². The activity of NiS_x/CF is better than that of the RuO₂/NF-Pt/C couple (1.55 V) and the recently reported bifunctional electrocatalysts such as MoS₂-Ni₃S₂ nanoparticles/NF (1.56 V) [49], Ni_{1-x}Fe_x/C (1.58 V) [50], and Fe-doped CoP nanoarray/Ti mesh (1.60 V) [51].

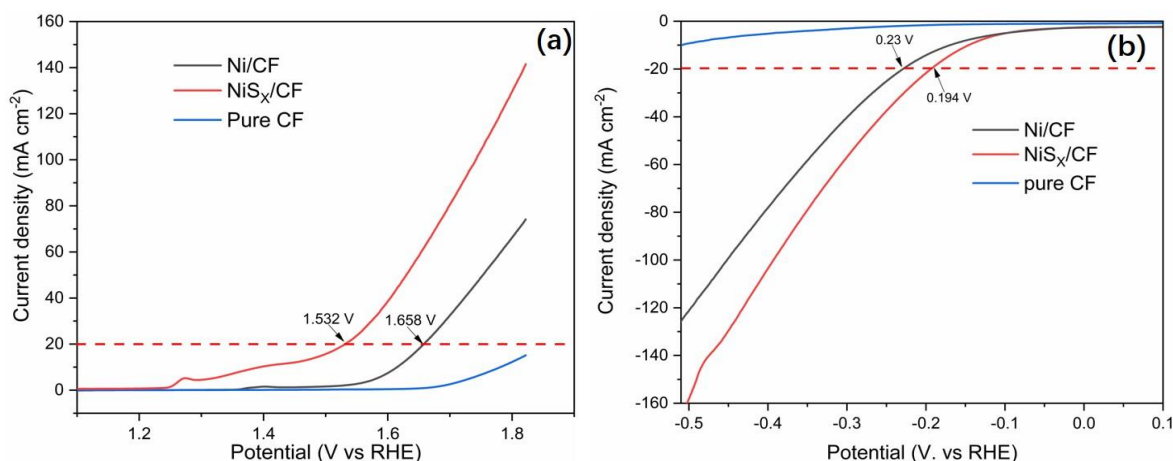


Figure 5. (a,b) Polarization curves of NiS_x/CF, Ni/CF and Pure CF for water splitting in 1.0M KOH.

Electrochemically active surface area (ECSA) is a main factor for the electrochemical reactivity that is determined by measuring the double layer capacitance (C_{dl}) at the electrolyte-electrode interface with the cyclic voltammetry [52]. The CVs of the catalyst NiS_x/CF are tested at different scanning rates from 20 to 200 mV s⁻¹ Fig. 6(a). The ECSA of NiS_x/CF was investigated using the C_{dl} that was found from the measured capacitances as shown in Fig.(7b). The results are shown in Fig. 6(b, c), the NiS_x/CF has a much higher C_{dl} (0.156 mF cm⁻²) and ECSA (3.9 cm²) than Ni/CF C_{dl} (0.067 mF cm⁻²) and ECSA (2.6 cm²) and Pure CF C_{dl} (0.039 mF cm⁻²) and ECSA (1 cm²). This high ECSA of NiS_x/CF primarily resulted from the massive active sites on the surface. The results show that the structure not only results in more effective exposure of catalytic activity sites, but also advances rapid electron transfer and ion diffusion, hence enhancing catalytic activity. The electronic interaction between the S and Ni changes the original electronic structure, which facilitates the water splitting [53].

Next, the main factor responsible for the enhanced catalytic activity is the Electrochemical impedance spectra (EIS). As depicted in Fig. 6(d) the NiS_x/CF has the smallest value of charge transfer resistance (18.68 Ω), which displays that NiS_x/CF has faster electron transfer rate compared to that of Ni/CF (22.71 Ω). The rapid electron transfer ability can effectively promote the combination of electrons and H_{ads}. The results imply an important enhancement in the catalytic activity of the Ni/CF after S doping. Meanwhile, according to the Nyquist plots, the smaller the radius, the lower is the charge-transfer resistance at the electrode interface [12]. Therefore, NiS_x/CF has faster charge transfer and kinetics. This result manifests that the electrode dynamics is basically to control the charge transfer process and the electrochemical system is approximated by the modified Randles circuit. The potential dependencies of the obtained data, include solution resistance (R_s), charge-transfer resistance (R_{ct}), and constant-phase element related to the double-layer capacitance (C_{dl}) [54]. To this end, resistances acquired from the EIS spectra of the various catalysts revealed that the NiS_x/CF catalyst had importantly lower impedance and, thus, markedly enhanced OER and HER kinetics.

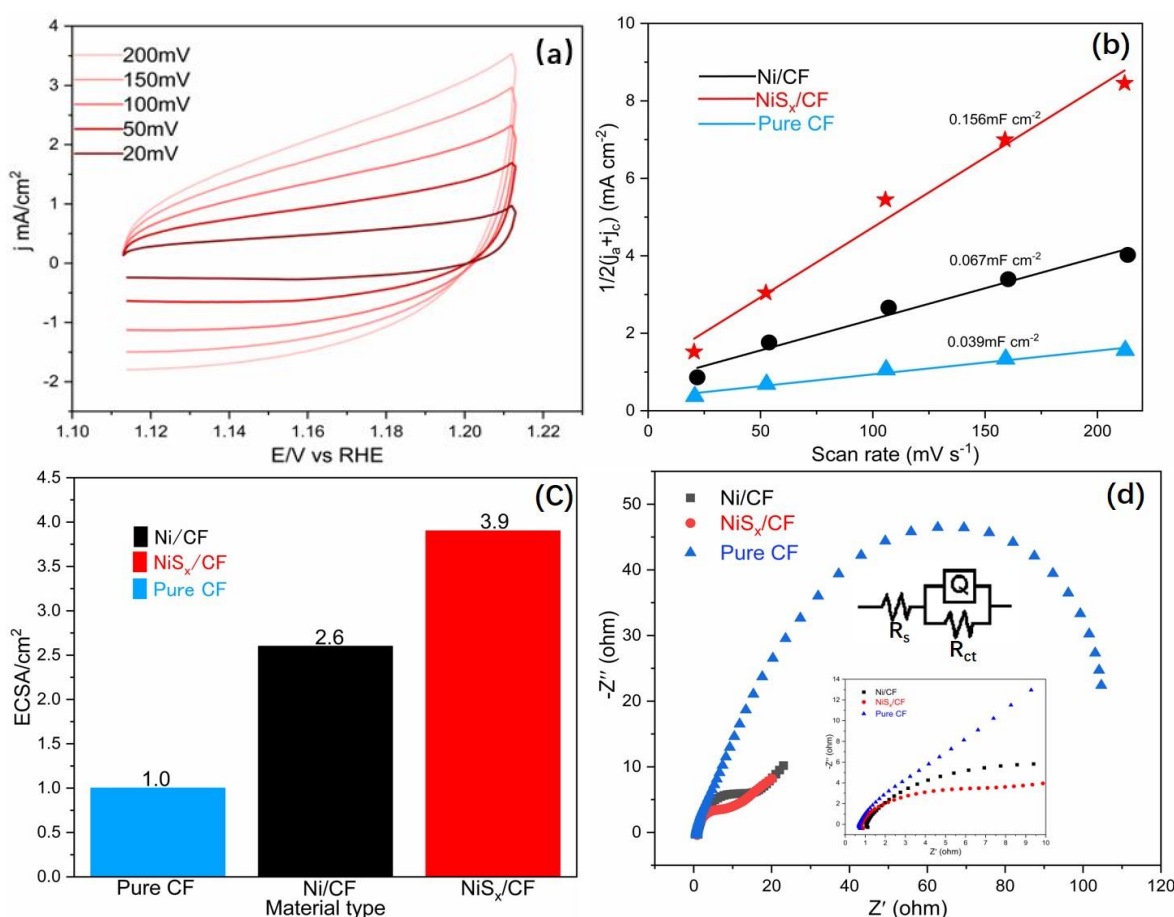


Figure 6. CVs recorded in a non-faraday region (1.11-1.21 V vs RHE) for NiS_x/CF. (b) The relationship between charging current density difference $1/2(j_a + j_c)$ and scanning rate is shown in the figure. The slope is C_{dl}. (c) Electrochemically active surface area (ECSA) comparison diagram. (d) Nyquist plots for the NiS_x/CF, Ni/CF and pure CF.

The long-term electrochemical stability is also an important factor for the water splitting catalyst. Fig. 7 shows a multistep chronopotentiometric curve for NiS_x/CF with a current density ranging from

10 to 80 mA cm^{-2} (10 mA cm^{-2} per 500 s). In the range of 1.64-1.90 V, all steps are kept unchanged for 500 seconds, which demonstrate that these process responses reflect the superb mass transport properties (outwards diffusion of oxygen bubbles and inward diffusion of OH^-) and (outwards diffusion of hydrogen bubbles and inward diffusion of H^+) [16]. conductivity and stability of the NiS_x/CF catalyst. This suggests that the NiS_x/CF is conditioned to serve as a high effective catalyst for water splitting.

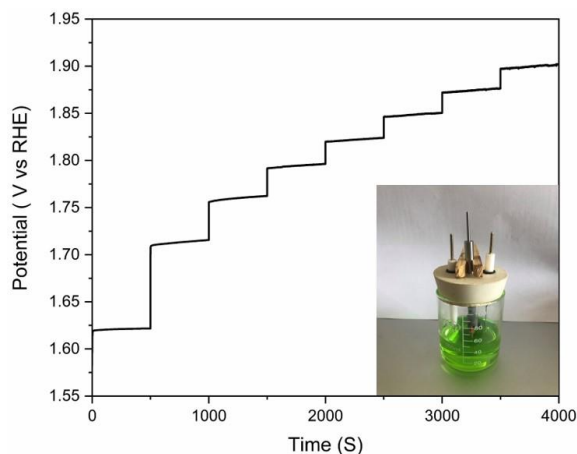


Figure 7. Multi-current process obtained with the NiS_x/CF catalyst. The current density started at 10 mA cm^{-2} and ended at 80 mA cm^{-2} , with an increment of 10 mA cm^{-2} every 500 s.

4. CONCLUSIONS

In summary, S-doped nickel microspheres directly grown on a copper foam act as highly effective catalysts for the water splitting using a one-step electrodeposition. Even though copper foam itself does not make a difference in these reactions, after being doped with nonmetal element (S), it shows reasonably good performance for water splitting. By doping with transition metals, the activity of the catalysts can be further improved. The NiS_x/CF exhibits remarkable electrochemical properties, requiring 146 mV of overpotentials to provide a current density of 10 mA cm^{-2} and 302 mV of overpotentials to provide a current density of 20 mA cm^{-2} for the HER and OER, respectively. The results also show that the NiS_x/CF catalyst only need 1.532 V to yield a current density of 20 mA cm^{-2} . The OER and HER performance was exhibited with a small Tafel slope of $120.1 \text{ mV dec}^{-1}$, and $156.2 \text{ mV dec}^{-1}$ respectively. Furthermore, the NiS_x/CF catalyst has the characteristic of maintaining stability at multiple potentials. Thus, NiS_x/CF can be a prospective effective electrocatalysts for water splitting. The increase in the catalytic performance of NiS_x/CF can be ascribed to the two main factors: (1) 3D porous structure of the NiS_x/CF favors the exposure of more active sites and (2) The nickel sulfur elements have a certain catalytic performance.

ACKNOWLEDGEMENTS

The authors acknowledge the support from Research is funded by the Natural Science Foundation of China (Project No. 51874154), of Kunming University of Science and Technology.

NOTES

The authors declare no competing financial interest

References

1. S. Han, S. Liu, R. Wang, *ACS Appl. Mater. Interfaces*, 9 (2017) 17186.
2. J. Lu, T. Xiong, W. Zhou, *ACS Appl. Mater. Interfaces*, 8 (2016) 5065.
3. D. Xiong, Q. Zhang, S. M. Thalluri, *Chem. - Eur. J.*, 23 (2017) 8749.
4. L. Zhang, J. Xiao, H. Wang, *ACS. Catal.*, 7 (2017) 7855.
5. J. Chi and H. Yu, *Chin. J. Catal.*, 39 (2018) 390.
6. Y. Ruan, C. Wang, J. Jiang, *J. Mater. Chem. A.*, 4 (2016) 6307.
7. S. Chu, A. Majumdar, *Nat.*, 488 (2012) 294.
8. A. Dutta, N. Pradhan, *J. Phys. Chem. Lett.*, 8 (2016) 144.
9. S. E. Hosseini, M. A. Wahid, *Renewable Sustainable Energy Rev.*, 57 (2016) 850.
10. J. Zhang, L. Lv, Y. Tian, *ACS Appl. Mater. Interfaces*, 9 (2017) 33833.
11. N.-T. Suen, S.-F. Hung, Q. Quan, N. Zhang, *Chem. Soc. Rev.*, 46 (2017) 337.
12. Y. Jiao, Y. Zheng, M. Jaroniec, *Chem. Soc. Rev.*, 44 (2015) 2060.
13. M. Tahir, L. Pan, F. Idrees, *Nano Energy*, 37 (2017) 136.
14. R. V. Mom, J. Cheng, M. T. M. Koper and M. Sprik, *J. phys. chem. C.*, 118 (2016) 4095.
15. X. Du, Q. Shao, X. Zhang, *Dalton Trans.*, 48 (2019) 1322.
16. C. Lu, C. Zhao, *Nat. Commun.*, 6 (2015) 6616.
17. Y. Pei, Y. Yang, F. Zhang, *ACS Appl. Mater. Interfaces*, 9 (2017) 31887.
18. C. Yang, C. Laberty-Robert, D. Batuk, *J. Phys. Chem. Lett.*, 8 (2017) 3466.
19. X. Bo, Y. Li, R. K. Hocking, *ACS Appl. Mater. Interfaces*, 9 (2017) 41239.
20. W. Ho, C. Y. Jimmy and S. Lee, *J. solid state chem.*, 179 (2006) 1171.
21. J. Tian, N. Cheng, Q. Liu, *J. Mater. Chem. A.*, 3 (2015) 20056.
22. L. Chai, W. Yuan, C. Xue, *RSC Adv.*, 8 (2018) 26871.
23. H. Du, R. Kong, F. Qu, *Chem. Commun.*, 54 (2018) 10100.
24. W. Zhou, X. J. Wu, X. Cao, *Energy Environ. Sci.*, 6 (2013) 2921.
25. Y. Wenyu, C. Laifei, A. Yurong, *ACS Sustainable. Chem. Eng.*, 6 (2018) 8976.
26. S. Zhao, Y. Wang, J. Dong, *Nat. Energy*, 1 (2016) 16184.
27. C. C. L. Mccrory, S. Jung, J. C. Peters, *J. Am. Chem. Soc.*, 135 (2013) 16977.
28. J. Zeng, M. Gao, Q. B. Zhang, *J. Mater. Chem. A.*, 5 (2017) 15056.
29. C. Xu, S. Peng, C. Tan, H. Ang, H. Tan, H. Zhang and Q. Yan, *J. Mater. Chem. Xu C.*, 2 (2014) 5597
30. C. Wan and B. M. Leonard, *Chem. Mater.*, 27 (2015) 4281.
31. J. Zhou, M. Caban-Acevedo, H. Liang, L. Samad, Q. Ding, Y. Fu, M. Li and S. Jin, *ACS Catal.*, 5 (2015) 6355.
32. F. Song, X. Hu, *J. Am. Chem. Soc.*, 136 (2014) 16481.
33. A. Sarkar, D. Seth, M. Jiang, *Top. Catal.*, 57 (2014) 730.
34. S. Mu, D. Wu, Y. Wang, *ACS Appl. Mater. Interfaces*, 2 (2010) 111.
35. L. L. Feng, G. Yu, Y. Wu, *J. Am. Chem. Soc.*, 137 (2015) 14023.
36. R. Sabela, I. Paseka, *J. Appl. Electrochem.*, 20 (1990) 500.
37. S. Kim, H. B. Pyo, S. H. Ko, *Langmuir*, 26 (2010) 7355.
38. Y. He, X.-P. Han, D.-W. Rao, Y.-D. Zhang, J. Zhao, C. Zhong, W.-B. Hu, W.-F. Wei and Y.-D. J. N.

- E. Deng, *Nano Energy.*, 61 (2019) 267.
39. Y. Zheng, Y. Jiao, Y. Zhu, Q. Cai, A. Vasileff, L. H. Li, Y. Han, *J. Am. Chem. Soc.*, 139 (2017) 3336.
40. A. Olivas, J. Cruz-Reyes, V. Petranovskii, *J. Vac. Sci. Technol., A*, 16 (1998) 3515.
41. M. García-Mota, M. Bajdich, V. Viswanathan, A. Vojvodic, *J. Phys. Chem. C.*, 116 (2012) 21077.
42. L. A. D. Faria, J. F. C. Boodts, S. Trasatti, *J. Appl. Electrochem.*, 26 (1996) 1195.
43. Y. Zhao, R. Nakamura, K. Kamiya, *Nat. Commun.*, 4 (2013) 2390.
44. K. Zhang, W. Wang, L. Kuai, *Electrochim. Acta*, 225 (2017) 303.
45. J. Ding, S. Ji, H. Wang, H. Gai, F. Liu, *R. Int. J. Hydrogen Energy*, 44 (2019) 2832.
46. L. N. Zhang, S. H. Li, H. Q. Tan, S. U. Khan, Y. Y. Ma, H. Y. Zang, Y. H. Wang, *ACS Appl. Mater. Interfaces*, 9 (2017) 16270.
47. Y. Li, H. Wang, L. Xie, *J. Am. Chem. Soc.*, 133 (2011) 7296.
48. C. C. Hou, C. J. Wang, Q. Q. Chen, X. J. Lv, *Chem. Commun.*, 52 (2016) 14470
49. N. Jiang, B. You, M. Sheng and Y. J. C. Sun, *Chem Cat Chem.*, 8 (2016) 106.
50. W. Zhu, X. Yue, W. Zhang, *Chem. Commun.*, 52 (2016) 1486.
51. J. Zhang, T. Wang, D. Pohl, *Angew. Chem.*, 55 (2016) 6702.
52. X. Zhang, H. Xu, X. Li, *ACS Catal.*, 6 (2015) 580.
53. C. Tang, R. Zhang, W. Lu, L. He, X. Jiang, A. M. Asiri and X. J. A. m. Sun, *J. Mater. Chem. A.*, 29 (2017) 1602441.
54. M. A. R. Anjum, J. S. Lee, *ACS Catal.*, 7 (2017) 3030.